

Self-Powered Gyroscope Angle Sensor Based on Resistive Matching Effect of Triboelectric Nanogenerator

Xinkai Xie, Yunfeng Chen, Jinxing Jiang, Junyan Li, Yanqin Yang, Yina Liu, Li Yang, Xin Tu, Xuhui Sun, Chun Zhao,* Mingchao Sun,* and Zhen Wen*

Gyroscope is one of the most widely distributed and utilized motion sensors among Internet of Things sensing for sports health, artificial intelligence, military management, civil defense, etc. Preparing a thoroughly self-powered gyroscope sensor based on triboelectric nanogenerator (TENG) with superior stability is of innovative research significance. In this work, a self-powered gyroscope angle sensor (SGAS) based on resistive impedance matching effect of TENG is proposed to detect relative rotation angle, performing as an attitude indicator applied in the flight control system of the unmanned aerial vehicle. The ultrahigh sensitivity of 67.3 mV deg^{-1} and outstanding linearity between the output voltage and rotation angle are obtained. Moreover, an instantaneous response within 20 ms can be observed during the process when gradually increasing the rotation angle from 0° to 260° . By lighting up different light-emitting diode patterns representing certain rotation angles, demonstrations on quantitative sensing alerts are also realized. The SGAS can operate without batteries or monitoring circuits, accompanied with excellent reliability and sensitivity, which is favorable for future automatic navigation control systems.

1. Introduction

Progressive improvements of the Internet of Things (IoT) promote the sustainable development of the modern information society.^[1,2] When the IoT is an analogy to the human sense as a means to immediately acquire precise environmental information, the large-scale and widely distributed sensor networks are similar to synaptic terminals, which are available to accurately realize various functions of intelligent identification, positioning, tracking, monitoring, and management. Among them, motion sensors, such as accelerometer, tilt sensor, vibration sensor, and rotation sensor, are widely utilized in health care, civil defense, industrial production, and home security.^[3–5]

Gyroscope is one of the most widely used motion sensors, which is dependent on the inertia to make the rotating shaft of the gyroscope rotor maintain a fixed direction under high-speed rotating motion

and simultaneously measure the angular movement.^[6,7] After incorporating the signal processing circuit, the gyroscope could not only realize the artificial intelligence health monitoring, for example, evaluating the patient's exercise ability after treatment, analyzing and testing the training performance of the athletes but also be applied to military automatic control systems, for instance, monitoring the flying posture of drones and taking photos, detecting the trajectory of space shuttles, trains, and ships, and locating the precise positions of mine tunnels, missile silos, and oil base.^[8,9] Nowadays, there are mainly three types of gyroscope sensors, namely mechanical, optical fiber, and microelectromechanical system (MEMS) gyroscopes, providing information on motion variables such as acceleration, angle, tilt, and angular velocity.^[10,11] Although these gyroscopes have been employed in multiple scenarios in the air, ground, ocean, and space, an external power source is required for the energy supply, which suffers weak battery endurance. The gyroscopes could not operate continuously, since batteries are obliged to be substituted or recharged frequently. However, it is difficult to replace the battery under extreme weather and unique environments. Moreover, the enormous power supply system induces severe challenges to manufacturing the sensor networks for IoT in mass production.


Ubiquitous mechanical movements such as wind, tide, vibration, and human body motion could be exploited as a

X. Xie, Y. Chen, J. Jiang, Y. Yang, X. Sun, Z. Wen
Institute of Functional Nano and Soft Materials (FUNSOM)
Jiangsu Key Laboratory for Carbon-Based Functional Materials and Devices
Soochow University
Suzhou 215123, China
E-mail: wenzhen2011@suda.edu.cn

X. Xie, J. Li, Y. Liu, L. Yang, C. Zhao
School of Science
School of Advanced Technology
Xi'an Jiaotong-Liverpool University
Suzhou 215123, China
E-mail: chun.zhao@xjtlu.edu.cn

X. Xie, X. Tu
Department of Electrical Engineering and Electronics
University of Liverpool
Liverpool L69 3GJ, UK

M. Sun
Changchun Institute of Optics
Fine Mechanics and Physics
Chinese Academy of Sciences
Changchun 130033, China
E-mail: quanquanlzz@163.com

 The ORCID identification number(s) for the author(s) of this article can be found under <https://doi.org/10.1002/admt.202100797>.

DOI: 10.1002/admt.202100797

continuous energy supply.^[12,13] The triboelectric nanogenerator (TENG), a fundamentally novel technology proposed by Wang's Group, has witnessed rapid progress to convert mechanical energy into electrical energy as the power source.^[14] TENG-based self-powered motion sensors with different detection techniques have been extensively investigated in the recent years.^[15] Shi et al. reported a 3D symmetrical gyro ball based on the triboelectric effect that can effectively collect mechanical energy from human hand vibration, rotation, rolling, and percussion, realizing acceleration sensing for medical science and health care.^[16] A liquid metal-gated tribotronic transistor by coupling an metal-oxide-semiconductor field-effect transistor and an liquid metal-TENG is utilized as an electronic gradiometer to accurately measure oscillation angle for mechanical calibration.^[17] A cylindrical self-powered multifunctional sensor based on a translational-rotary magnetic mechanism is demonstrated to measure rotational parameters applied in sports.^[18] Furthermore, a self-powered arbitrary motion sensor based on electromagnetic-triboelectric composite transmits low-frequency (<5 Hz) motion data to the mobile phone through Bluetooth communication and presents a tilt angle sensitivity of 9.83 mV deg⁻¹.^[19] However, most of the mentioned self-powered motion sensors require an external monitoring circuit, which considerably increases the complexity of the sensing system. Additionally, the signal-to-noise ratio, sensitivity, and stability of the system should be carefully considered from design perspective and required further improvement. Therefore, preparing a thoroughly self-powered gyroscope motion sensor with superior stability and sensitivity is of significant research importance.

Recently, our group has proposed a reliable and completely self-powered sensing system based on the impedance matching effect of TENG.^[20–24] Due to the intrinsic capacitance of TENG, the voltage output of loaded traditional capacitive/resistive sensors changes significantly within a certain impedance interval, driving the alarm device to realize various physical and chemical

sensing detections. Technologies combined with the impedance matching mechanism offer a potential and promising solution to address the above challenges of motion sensors. Herein, a self-powered gyroscope angle sensor (SGAS) based on the resistive impedance matching effect of TENG is proposed as an attitude or heading indicator applied in the flight control system of the unmanned aerial vehicle (UAV). The proposed gyroscope angle sensing system includes a freestanding-mode rotary disc-shaped triboelectric nanogenerator (FRD-TENG) as an energy harvester, a resistive rotation angle sensor, and an light-emitting diode (LED) alert display. The relationship between voltage variation and rotation angle ranging from 0° to 260° is near-linear with ultrahigh sensitivity of 67.3 mV deg⁻¹. Moreover, the employed sensing system demonstrates the quantized LED pattern alarm function representing different rotation angles without batteries and management circuits. It possesses the capability for accurate angle measurements, exhibiting broad application prospects in the fields of UAV navigation, autonomous driving, etc.

2. Results and Discussion

The conceptual scheme of the air-driven SGAS applied in UAV as an attitude or heading indicator is illustrated in **Figure 1a** and the photograph of the SGAS model is shown in Figure S1 in the Supporting Information. In general, the SGAS contains three parts: a freestanding-mode rotary disc-shaped, a resistive rotary potentiometer (RRP), and an LED alert display. Pneumatic air-powered FRD-TENG enhances safety in case the conventional electric mode breaks down. For UAV, the aerodynamic force comes from the ambient wind blowing, while for helicopters or airplanes that require a large amount of energy, the engine-driven vacuum pump can suckle filtered air from the cabin to drive the FRD-TENG. To certify the SGAS operating regularly, the rotator of the FRD-TENG retains periodic rotary movement at a high velocity,

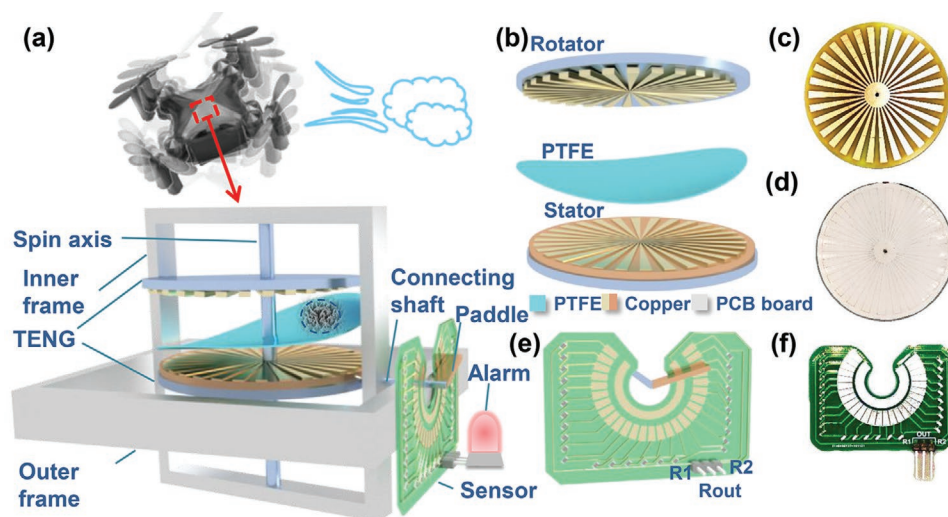


Figure 1. Conceptual illustration of self-powered gyroscope angle sensing system. a) Scheme of the air driven self-powered gyroscope angle sensor (SGAS) applied in the unmanned aerial vehicle (UAV) as an attitude or heading indicator, which consists of a freestanding-mode rotary disc-shaped triboelectric nanogenerator (FRD-TENG) as power supply, a resistive rotary potentiometer (RRP), and LED alert display. b) Structural design of the FRD-TENG, including rotator, stator, and triboelectrification layer of PTFE. c) Photographs of the rotator patterned with a radial copper electrode and d) the complementary stator sector covered by PTFE film. e) Schematic illustration and f) digital photograph of the RRP with a monitoring range of 0°–260°.

which is simulated by adjusting the rotation speed of the rotating motor. On one hand, the rotator of FRD-TENG rotates around the spin axis, that is to say, the plane of rotating FRD-TENG is parallel to the horizontal plane, which maintains the direction when the UAV fuselage undergoes angular deflection, such as pitch and roll. On the other hand, the stator of FRD-TENG is connected to the guided paddle of RRP by the connecting shaft to provide flight orientation. As shown in Figure 1b, the FRD-TENG is prepared with a multilayer structure, which mainly consists of a rotor and a stator. The rotator includes a radial array of copper electrodes with 30 equally distributed sectors each having a spacing angle of 6° . Besides, the stator section consists of two supplemental circular interdigital electrodes printed as patterns on an industrially fabricated printed circuit board (PCB), covered by the plasma etching processed poly(tetrafluoroethylene) (PTFE) film acting as the triboelectric layer. The digital photographs of the rotator and stator with a radius of 57 mm are depicted in Figure 1c,d. The structure illustration of the RRP is shown in Figure 1e, which is composed of a nonintegral circular thin film resistor split into 27 segments, a ring-shaped metal electrode, and a copper guide paddle. Figure 1f presents the digital photograph of the RRP with a resistance variable from 1 to 3.6 M Ω . The RRP is fixed to the outer frame of the SGAS and connected in series with an LED warning light. As demonstrated in the simulation animation Movie S1 in the Supporting Information, the outer frame of the UAV sway from side to side during the flight due to gravity, causing the copper paddle to slide between 0° and 260° . Based on the resistive impedance matching effect of the FRD-TENG, the load resistance of the FRD-TENG changes during outer frame rotation, thus the LED alarm could dynamically detect the flight attitude of the UAV by indicating the deflection angle.

Toward the typical FRD-TENG, which is a fundamental application of Maxwell's displacement current, the operating mechanism is based on the coupling of contact electrification and electrostatic induction.^[25,26] A description of the charge transfer and current flow process through one individual district of the FRD-TENG with a load resistance is presented in Figure 2ai. Two independent moments when the rotator sector is perfectly aligned with the corresponding parts of electrode 1 and electrode 2 on the stator are defined as the initial and final states, respectively. Meanwhile, the transition moment from the initial state to the final state is described as the intermediate state. Primitively, the rotator comes into contact with the PTFE film generating positive charges on the copper electrode 1 and an equivalent amount of negative charges on the PTFE surface. Following a relative rotation of the rotor and stator causes free electrons to flow from electrode 2 to electrode 1. Aiming to intuitively demonstrate the potential differences during the rotation process, we utilized the COMSOL software to calculate the induced potential distribution in the open-circuit condition, as shown in Figure 2aai. An analytical model is built considering the overlap between the rotator and the stator as a capacitor with the assumption that the edge effect is neglectable. Therefore, the open-circuit voltage (V_{oc}) can be analytically expressed by the following equation using the Gauss theorem

$$V_{oc} = \frac{2d \cdot \sigma}{\epsilon_0 \epsilon_r} \quad (1)$$

where d is the thickness of the PTFE layer, ϵ_0 is the vacuum dielectric constant, and ϵ_r is the relative dielectric constant of PTFE.

A rotating motor was utilized to accurately control the rotation rate of the rotator and the electrical output performance of the FRD-TENG was measured by an electrometer. As shown in Figure 2b–d, when the rotation speed increases from 30 to 150 rpm, the open-circuit voltage (V_{oc}), and the transferred charge amount remain almost constant at 108 V and 80 nC, respectively, while the short circuit current (I_{sc}) increases proportionally from 3.49 to 15.10 μ A. Moreover, the influence of the external load resistance on the peak output power of the FRD-TENG at different rotation speeds is explicated in Figure 2e. At various rotation speeds, the peak output power increases at the initial stage to the maximum value and gradually decreases with the increasing of the external load resistance ranging from 20 to 200 M Ω . Derived from previous mathematical analysis, the optimal load resistance is inversely proportional to the average motion frequency of TENG.^[27] The experimental results are consistent with this inference. From the view of longitudinal analysis, the matching resistance corresponding to the vertex of peak power output is inversely proportional to the rotation frequency, as shown in Figure 2f. In detail, the matching resistance is 5 M Ω for frequencies at 30 and 60 rpm, 2 M Ω for frequencies at 90 and 120 rpm, and 1 M Ω for the frequency at 150 rpm. Besides, the current and voltage output characteristics with different external load resistances at various rotation speeds are elucidated in Figures S2 and S3 in the Supporting Information, respectively. It is obvious that at the certain load resistance, with the increase of rotation speed, the partial voltage of FRD-TENG reduces due to decline of its inherent average impedance, while the output voltage of the load resistance increases. To specifically determine the resistance variation range of the RRP to be prepared, the medium rotation rate of 90 rpm was selected as a research condition. Previous research has shown that the TENG output voltage demonstrates three regions with different external load resistances and dramatically increases in the second region. Therefore, the resistance changing range of the connected sensor should be adjusted in the middle region to realize impedance matching induced self-powered sensing. As shown in Figure 2g, the output voltage increases significantly with the subsequent increasing load resistance from 0.1 to 20 M Ω in Region II. Within this range, the resistance changing interval of 1–10 M Ω , which exhibits apparent linearity, was chosen to further precise the resistance variation range of the sensor. Consequently, Figure 2h shows the relationship between voltage output and external resistance ranging from 1 to 10 M Ω . It can be observed that in the range of 1–3.6 M Ω , the output voltage increases linearly and remarkably with a rate of 6.73 V/M Ω , which is six times superior to the rate (1.06 V M Ω^{-1}) displaying in the range of 3.6–10 M Ω . Therefore, the optimal resistance changing range of the designed RRP can be preferably dominated between 1 and 3.6 M Ω .

Figure 3a illustrates the resistance variation on the RRP at different rotation angles. Increasing the rotation angle from 0 to 260° shifts the resistance of the RRP from 1 to 3.6 M Ω . Taking into account the influence of real environmental factors on the RRP, the resistance values under different temperatures and humidities were recorded. As depicted in Figure 3b, the

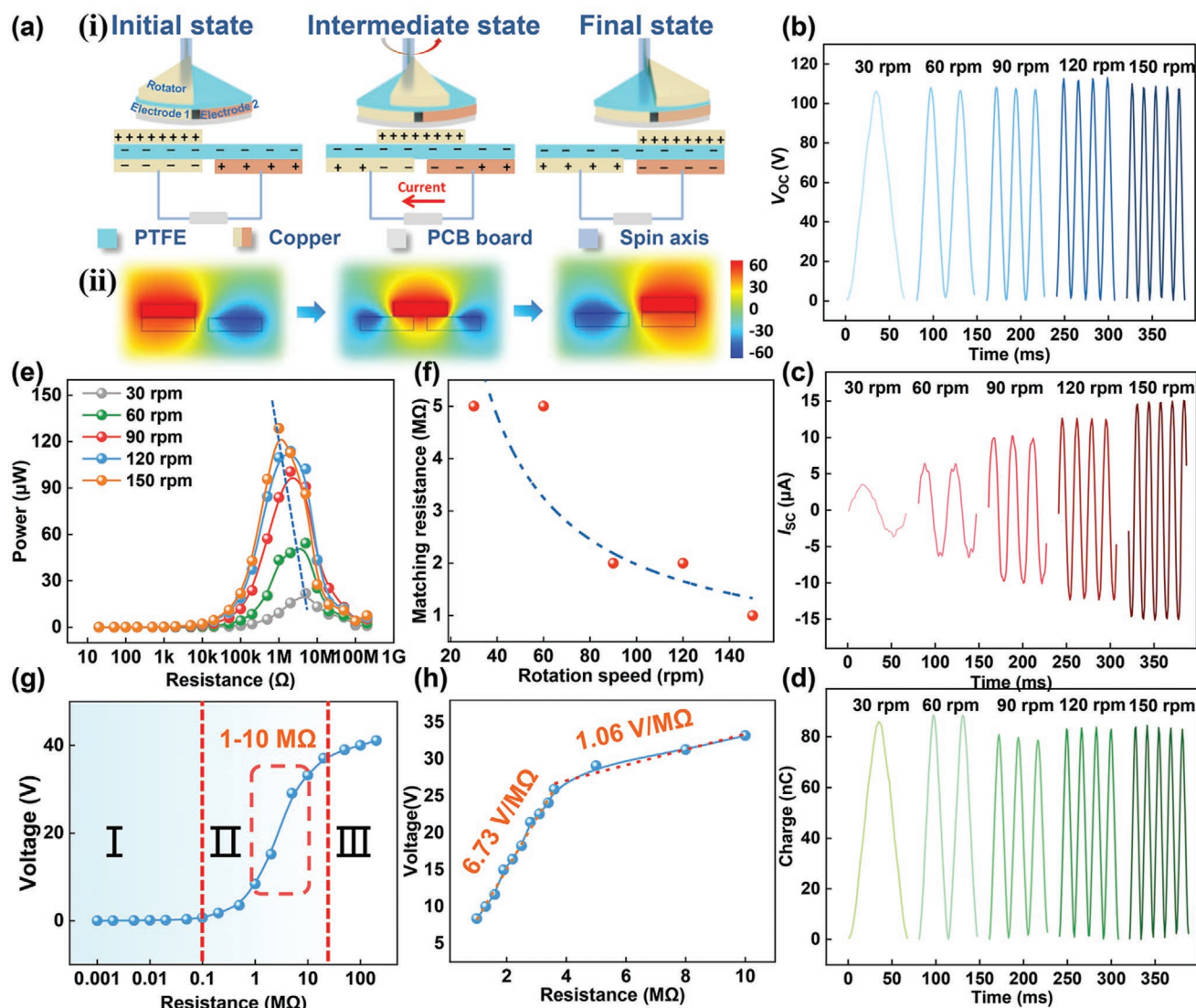


Figure 2. Working mechanism and resistive impedance matching effect of the FRD-TENG. a,i) Operating principle of the FRD-TENG. One sector of 6° from the rotator is chosen as to illustrate charge distribution during the rotating process. ii) COMSOL simulation on the surface potential during one rotation cycle. b) Open-circuit voltage (V_{oc}), c) short-circuit current (I_{sc}), and d) transferred charges (Q_{tr}) of the FRD-TENG working at different rotation speeds. e) Output peak power of the FRD-TENG with a variable load resistance. f) Matching load resistance corresponding to the maximum peak power obtained at different rotation speeds. g) Relationship between output voltage and load resistance at the rotation speed of 90 rpm and h) the enlarged diagram to display the output linear fitting result with load resistance ranging from 1 to 10 M Ω .

resistance value maintains about 1.9 M Ω at a rotation angle of 90° when increasing the temperature from 10 to 80°C . Likewise, the resistance remains stable as the humidity changes from 20% to 80%. Furthermore, multiple measurements have confirmed that the resistance fluctuation difference does not exceed 2%, indicating excellent stability that can adapt to extreme weather conditions. Based on the resistive impedance matching effect of TENG, an SGAS was built by connecting the RRP with the FRD-TENG in series, along with an electrometer to measure the output voltage of the RRP. Figure 3d illustrates the equivalent circuit for electrical measurements of the SGAS. All the measurements were conducted at a rotation speed of 90 rpm. Figure 3e shows the corresponding voltage values of the SGAS at various rotation angles. With the increase of the

rotation angle from 0° to 260° , the voltage surges linearly from $\approx 8.4 \text{ V}$ to $\approx 26 \text{ V}$. A sensitivity of 673 mV deg^{-1} was acquired for the linear fitting relation with an R^2 value of 99.08%. Figure 3f illustrates the real-time output voltage profile on the SGAS when rotating across three-quarter arcs within 2 s. Meanwhile, the enlarged image on the right side shows the increase in peak voltage within 20 ms. Given that the bandwidth of the two adjacent voltage peaks is $\approx 20 \text{ ms}$, the SGAS is considered to have notable sensitivity for real-time sensing. Moreover, the reliability of the response–recovery performance has been investigated, as shown in Figure 3g. During six cycles turning the outer frame from 0° to 90° , the output voltage increases rapidly from 8.4 to 15 V every time and can completely recover to the initial value within 0.3 s after rotating reversely to the starting

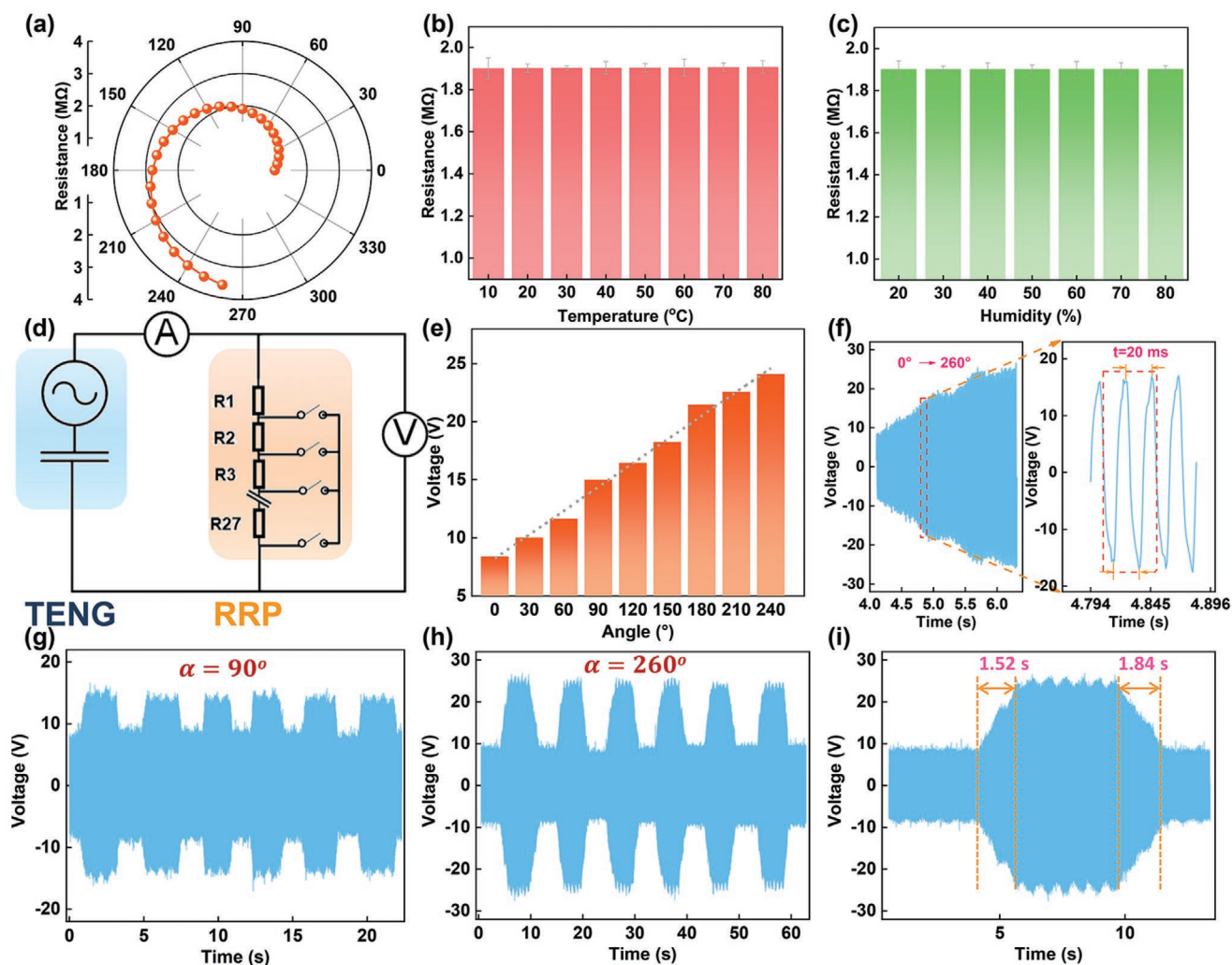


Figure 3. General characterization of the RRP and typical performance of the self-powered rotation angle sensor. a) Relationship between resistance value and rotation angle of the RRP. b) Resistance stability under different temperature and c) humidity environments at a rotation angle of 90°. d) Equivalent circuit diagram of the designed self-powered gyroscope angle sensor. e) Near-linear relationship between voltage variation and rotation angle ranging from 0° to 240°. f) Real-time response profile of voltage augmentation when increasing the rotation angle. g) Response–recovery cycle measurements of dynamic voltage output profiles at the rotation angle of 90° and h) 260°. i) Enlarged view to illustrate the response and recovery processes.

point, which validates outstanding stability of the SGAS. Similarly, excellent repeatability on the response–recovery curve of the output voltage can also be observed in Figure 3h,i. When rotating the outer frame from 0° to the maximum angle of 260°, the output voltage instantly increases from 8.4 to 26 V within 1.52 s and then decreases to the original value within 1.84 s, demonstrating the capability of fast response and reliable stability. For broader application scenarios, the rotation angle sensing range could be extended from 0° to nearly 360° by designing the continuous circular electrode, fan-shaped copper electrode groups, and multiple resistors of RRP arranged into a whole circular shape. By decreasing the separation angle of the two resistors to 5°, 2°, or 1°, the sensing resolution could be greatly improved.

For practical application demonstration, the SGAS can be utilized for rotation angle sensing and alarming. In Figure 4a, the

equivalent circuit diagram of the self-powered angle quantitative alarm sensing system was demonstrated, which includes three parts: the FRD-TENG, the RRP, and different LED patterns regulated by the sliding switch K1, K2, and K3. Correspondingly, the digital photograph of the quantitative sensing system was shown in Figure 4b. The relative angle between the outer frame and the inner frame is defined as the rotation angle α , as illustrated in the magnified image. In Figure 4c, the real-time output voltage response of the SGAS when the copper paddle pointing to different angles is variably depicted. When $\alpha = 0^\circ$, 90° , and 180° , the simultaneous AC output voltages are 8.4, 15, and 21.5 V, respectively. To demonstrate the self-powered angle quantitative alarm sensing system, a rotating motor was utilized to actuate the rotator of the FRD-TENG and control the rotation speed at 90 rpm. For further explanation, the threshold voltage of each emerald green LED is ≈ 2 V, thus each LED pattern

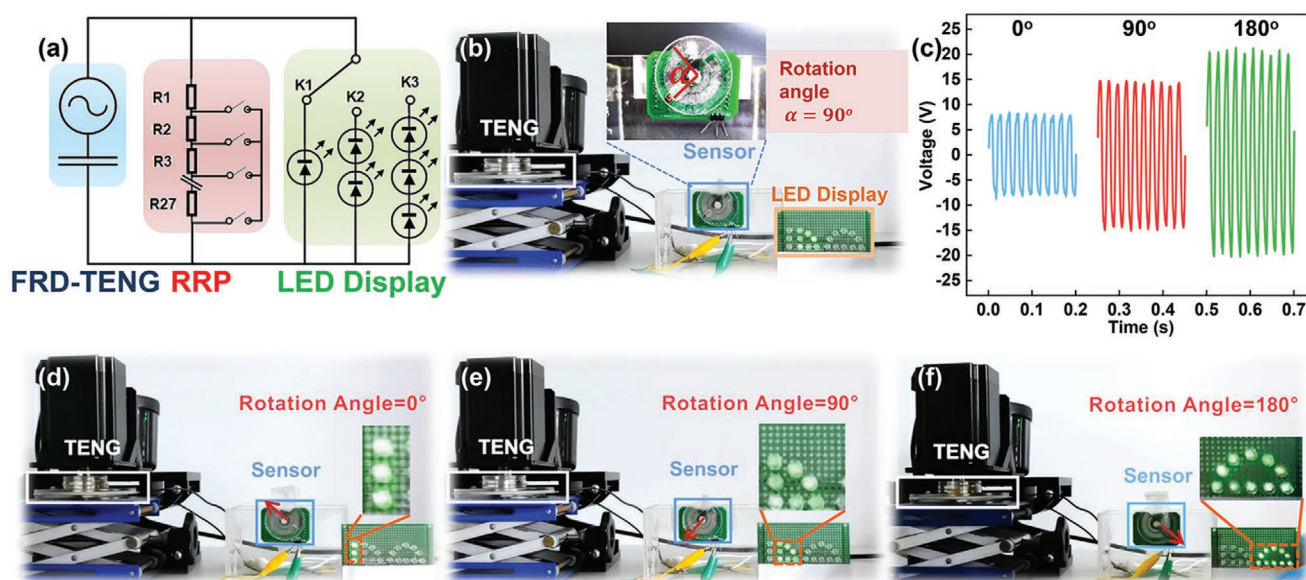


Figure 4. Demonstration of self-powered gyroscope angle sensing system. a) Equivalent circuit diagram and b) digital photograph of the self-powered angle quantitative alarm sensing system. c) Output voltage performance when relative rotation angle $\alpha = 0^\circ$, 90° , and 180° . Photograph of the quantitative sensing presentation with d) the first column of lights is lit when $\alpha = 0^\circ$, e) the second column of lights is lit when $\alpha = 90^\circ$, and f) the third column of lights is lit when $\alpha = 180^\circ$.

requires specific voltages to light up. The LED patterns representing 0° , 90° , and 180° are composed of three, seven, and ten green LEDs, indicating that the expected working voltages are ≈ 6 , ≈ 14 , and ≈ 20 V, respectively. When the rotation angle α increases, the resistance of the SGAS increases gradually which leads to the raise of the peak output voltage and the number of LEDs lighted on. Figure S4 in the Supporting Information shows the output voltage performance at various relative rotation angles. To indicate the flight status of UAV vividly, the LED patterns were arranged in a shape corresponding to the angle. As shown in Figure 4d, only three LEDs can be lighted at a rotation angle of 0° . From Figure 4e that seven LEDs can be easily lighted when increasing the rotation angle to 90° . Moreover, ten LEDs can be lighted if further increasing the rotation angle to 180° (Figure 4f), realizing quantitative sensing alerts for different attitudes. Movie S2 in the Supporting Information presents the demo of the self-powered quantifiable angle sensing system. By controlling the motor rotation speed at 90 rpm, the LEDs displayed in different shapes can be lighted on when rotating to corresponding angles at 0° , 90° , and 180° . As a consequence, the SGAS by coupling of triboelectric and resistive effects exhibits a broad application prospect in UAV attitude indicator.

3. Conclusion

In conclusion, a self-powered gyroscope angle sensor based on resistive impedance matching effect of TENG containing a typical FRD-TENG, a resistive rotation potentiometer was introduced and demonstrated to measure the rotation angle as an attitude indicator applied in the flight control system of the unmanned aerial vehicle. Ultrahigh sensitivity of 67.3 mV deg^{-1}

and excellent linearity between the output voltage and rotation angle were obtained when rotating from 0° to 260° . Furthermore, the difference between two adjacent output voltages can be observed within 20 ms, representing the transient response function. In addition, quantized alarming has been achieved by introducing switch-controlled LED arrays, which demonstrated that LED patterns representing “ 0° ,” “ 90° ,” and “ 180° ” can be lighted up when the relative rotation angle α equals to the corresponding value. Compared with current commercial MEMS sensors, it is feasible to tweak the SGAS for experiment and application requirements easily in lab and test immediately once finished tweaking. There is no need to spend extra money and time for a new tape out like MEMS devices. It is also possible to install multiple SGASs in different planes, providing more comprehensive information on pitch, bank, and yaw. The SGAS without external batteries or management circuits shows great application prospect in IoT sensing, as an attitude or heading indicator for the UAV navigation and autonomous driving, especially revealing outstanding advantages under conditions of cloud cover, poor visibility, and night flying.

4. Experimental Section

Fabrication of the FRD-TENG: The structure of the TENG includes three main parts: the stator, the rotor, and the triboelectric PTFE layer. First, the PCB plate with sector-shaped copper electrodes is used as the rotor, which is also regarded as a triboelectric layer surface. Second, the PTFE film is stuck on the PCB plate with the interdigital copper electrodes as the stator, working as the other triboelectric layer. Finally, two conducting wires are led out on the back of the stator disk for access to the test platform. Among them, to obtain a higher power output, the current output needs to be further increased. According to the formula $I = dQ/dt$, the cycle time interval can be effectively reduced by reducing

the angle of the disc interval sector, so the small sector angle selected in this experiment is 6°.

Fabrication of the RRP: The RRP is mainly composed of three parts: a three-quarters circular copper electrode, 27 fan-shaped copper electrode groups arranged around the circular electrode, and a constant resistance between each fan-shaped electrode and the whole circular electrode. A copper sliding paddle is fixed to the central axis, which could rotate with the movement of the outer frame. As the rotation angle increases by 10°, a series resistor is connected to the circuit. Set $R_1 = 1\text{ M}\Omega$, thus the resistance value of the RRP is 1 M Ω when the rotation angle was 0°. Since the remaining R_2 – R_{27} is 0.1 M Ω for each, the RRP resistance increases by 0.1 M Ω every 10°. Figure S5 in the Supporting Information shows the linear relationship between the resistance value of the RRP and rotation angle under different initial resistances in the range of 1–2 M Ω and interval resistances of 0.1–0.2 M Ω . The resistance range of the RRP can be effectively modulated by adjusting the initial resistance and the interval resistance. In addition, the resolution of resistance changing with rotation angle can be improved by increasing the number of interval resistors.

Electrical Output Performance Characterization: A rotating motor was used to drive the rotor of the FRD-TENG to generate mechanical motion, and the rotation frequency is controlled by adjusting the rotating speed. The open-circuit voltage, short-circuit current, and transferred charges can be measured by connecting the two ends of TENG electrodes to the programmable electrometer (Keithley 6514). A desktop digital Volt/Ohm meter (DM3058E) was employed to measure the resistance value of the RRP.

Supporting Information

Supporting Information is available from the Wiley Online Library or from the author.

Acknowledgements

X.X., Y.C., and J.J. contributed equally to this work. This work was supported by the National Natural Science Foundation of China (NSFC) (61804103), Natural Science Foundation of the Jiangsu Higher Education Institutions of China Program (19KJB510059), the Suzhou Science and Technology Development Planning Project: Key Industrial Technology Innovation (SYG201924), the Key Program Special Fund in Xi'an Jiaotong-Liverpool University (XJTLU) (KSF-A-18), and China Postdoctoral Science Foundation (No. 2021T140494). This work was also supported by the Collaborative Innovation Center of Suzhou Nano Science and Technology, the 111 Project, and Joint International Research Laboratory of Carbon-Based Functional Materials and Devices.

Conflict of Interest

The authors declare no conflict of interest.

Data Availability Statement

Research data are not shared.

Keywords

gyroscope angle sensor, impedance matching, self-powered sensing, triboelectric nanogenerator

Received: July 1, 2021

Revised: July 20, 2021

Published online:

- [1] E. Borgia, *Comput. Commun.* **2014**, *54*, 1.
- [2] C. W. J. Li, I. Dharmasena, X. Ni, Z. Wang, H. Shen, S. L. Huang, W. Ding, *Intell. Converged Networks* **2020**, *1*, 115.
- [3] G. Wei, Y. Bi, X. Li, D. Xu, W. Xu, L.-J. Yang, Y. Qin, H. Guo, X. Zhao, X. Chen, L. Jia, *Nano Energy* **2018**, *54*, 10.
- [4] X. Pu, H. Guo, Q. Tang, J. Chen, L. Feng, G. Liu, X. Wang, Y. Xi, C. Hu, Z. L. Wang, *Nano Energy* **2018**, *54*, 453.
- [5] H. Lin, M. He, Q. Jing, W. Yang, S. Wang, Y. Liu, Y. Zhang, J. Li, N. Li, Y. Ma, L. Wang, Y. Xie, *Nano Energy* **2019**, *56*, 269.
- [6] J. Chung, H. Yong, H. Moon, D. Quang Van, S. T. Choi, D. Kim, S. Lee, *Adv. Sci.* **2018**, *5*, 1801054.
- [7] Y. Wu, Q. Jing, J. Chen, P. Bai, J. Bai, G. Zhu, Y. Su, Z. L. Wang, *Adv. Funct. Mater.* **2015**, *25*, 2166.
- [8] J. Wang, W. Ding, L. Pan, C. Wu, H. Yu, L. Yang, R. Liao, Z. L. Wang, *ACS Nano* **2018**, *12*, 3954.
- [9] H. Roh, J. Yu, I. Kim, Y. Chae, D. Kim, *ACS Appl. Mater. Interfaces* **2019**, *11*, 25170.
- [10] K. Dai, X. Wang, F. Yi, C. Jiang, R. Li, Z. You, *Nano Energy* **2018**, *45*, 84.
- [11] D. Choi, T. Sung, J.-Y. Kwon, *Adv. Mater. Technol.* **2018**, *3*, 1800219.
- [12] N. N. Zhai, Z. Wen, X. P. Chen, A. M. Wei, M. Sha, J. J. Fu, Y. N. Liu, J. Zhong, X. H. Sun, *Adv. Energy Mater.* **2020**, *10*, 2001041.
- [13] C. Chen, Z. Wen, J. Shi, X. Jian, P. Li, J. T. W. Yeow, X. Sun, *Nat. Commun.* **2020**, *11*, 4143.
- [14] Z. L. Wang, *Mater. Today* **2017**, *20*, 74.
- [15] Q. Miao, C. Liu, N. Zhang, K. Lu, H. Gu, J. Jiao, J. Zhang, Z. Wang, X. Zhou, *ACS Appl. Electron. Mater.* **2020**, *2*, 3072.
- [16] Q. Shi, H. Wu, H. Wang, H. Wu, C. Lee, *Adv. Energy Mater.* **2017**, *7*, 1701300.
- [17] T. Bu, D. Jiang, X. Yang, W. Liu, G. Liu, T. Guo, Y. Pang, J. Zhao, F. Xi, C. Zhang, *Adv. Electron. Mater.* **2018**, *4*, 1800269.
- [18] Z. Wu, B. Zhang, H. Zou, Z. Lin, G. Liu, Z. L. Wang, *Adv. Energy Mater.* **2019**, *9*, 1901124.
- [19] T. Bhatta, P. Maharjan, M. Salauddin, M. T. Rahman, S. M. S. Rana, J. Y. Park, *Adv. Funct. Mater.* **2020**, *30*, 2003276.
- [20] X. Xie, Y. Zhang, C. Chen, X. Chen, T. Yao, M. Peng, X. Chen, B. Nie, Z. Wen, X. Sun, *Nano Energy* **2019**, *65*, 103984.
- [21] X. Xie, Z. Wen, Q. Shen, C. Chen, M. Peng, Y. Yang, N. Sun, P. Cheng, H. Shao, Y. Zhang, Q. Zhu, X. Chen, X. Sun, *Adv. Mater. Technol.* **2018**, *3*, 1800054.
- [22] Q. Shen, X. Xie, M. Peng, N. Sun, H. Shao, H. Zheng, Z. Wen, X. Sun, *Adv. Funct. Mater.* **2018**, *28*, 1703420.
- [23] C. Chen, Z. Wen, A. Wei, X. Xie, N. Zhai, X. Wei, M. Peng, Y. Liu, X. Sun, J. T. W. Yeow, *Nano Energy* **2019**, *62*, 442.
- [24] Y. Zhang, M. Peng, Y. Liu, T. T. Zhang, Q. Q. Zhu, H. Lei, S. N. Liu, T. Yi, L. Li, Z. Wen, X. H. Sun, *ACS Appl. Mater. Interfaces* **2020**, *12*, 19384.
- [25] G. Zhu, J. Chen, T. Zhang, Q. Jing, Z. L. Wang, *Nat. Commun.* **2014**, *5*, 3426.
- [26] M. Bi, S. Wang, X. Wang, X. Ye, *Nano Energy* **2017**, *41*, 434.
- [27] S. Niu, Z. L. Wang, *Nano Energy* **2015**, *14*, 161.